applied sciences

MDPI

Article

Numerical and Experimental Analysis of Roller Hemming on Door Panel's Curved and Straight-Edge of Flat Plane

Chaohai Liu *,† and Weimin Lin †

Division of Mechanical Science and Technology, Faculty of Science and Technology, Gunma University, 1-5-1 Tenjin-Cho, Kiryu 376-8515, Japan

* Correspondence: t202b603@gunma-u.ac.jp

† These authors contributed equally to this work.

Abstract: Owing to its enhanced production efficiency, roller hemming has become the mainstream process for forming and joining metal sheets in the automotive industry. This study investigates the roller hemming process of a specific car door panel through a combination of experimental analysis and finite element analysis (FEA) on both straight-edge and curved-edge flat surfaces. Consequently, the mechanical properties of the door panel, including tensile strength, yield strength, modulus of elasticity, and Poisson's ratio, were estimated through tensile testing and then underwent finite element modeling. The simulation results demonstrated the varying distribution of stress during the rolling hemming process, with the highest stress concentration observed in the bending area. Additionally, creepage and growing results were acquired from both simulation and experimental data to validate the precision of the numerical model. A comparison was made between the experimental and simulation results of the external forces exerted by the roller on the panel. In both straight- and curved-edge sections, the external force during final hemming exceeded that during pre-hemming, as revealed by experimental measurements of both normal and tangential external forces, surpassing their corresponding simulated values.

Keywords: roller hemming; simulation; experiment; external force; creepage/growing

Citation: Liu, C.; Lin, W. Numerical and Experimental Analysis of Roller Hemming on Door Panel's Curved and Straight-Edge of Flat Plane. *Appl. Sci.* **2024**, *14*, 10066. https://doi.org/10.3390/app142110066

Academic Editor: Ana Martins Amaro

Received: 26 September 2024
Revised: 28 October 2024
Accepted: 30 October 2024
Published: 4 November 2024

1. Introduction

Hemming is a sheet metal joining process that involves folding outer panel edges onto the inner panel, which is vital in the automotive industry for superior visual quality. While hemming offers benefits, methods like die and table-top hemming incur high investment costs due to fixed tooling configurations [1]. This study focuses solely on roller hemming technology, as the development in the hemming field is oriented towards roller hemming. This technique has been widely used in the automotive industry to enhance the visual quality of closures, such as doors, hoods, sunroofs, tailgates, and wheel arches.

Most of the previous studies have focused on traditional tabletop hemming. The hemming process started in the 1980s. Hishida and Sato [2] investigated the hemming process using a plane strain model for simulation, and they found that warping easily happened in the final-hemming stage; after completing the final-hemming stage, the panel edges undergo a recoiling phenomenon upon the withdrawal of the hemming force. Livatyali et al. [3] employed a numerical model and performed experiments to investigate the impact of various flanging and hemming parameters, including different flanging heights and plate radii of curvature, on the quality of table hemming, specifically focusing on metal creep, warpage, and recoil. The authors utilized aluminum-killed drawing quality (AKDQ) steel for the upper plate material and baked hard enabled (BH) steel for the lower plate material. Furthermore, Zhang Guohua et al. [4] assessed the occurrence of recoil and surface warp during the flat surface, straight-edge hemming process. The authors concluded that reverse bending and springback were the fundamental mechanisms

behind surface warp and recoil and are not independent of hemming quality. The authors also evaluated the recoil and warp after the final-hemming stage and found that the pre-hemming angle had a significant effect on the final surface warp. Additionally, Zhang and Hao [5] investigated the hemming quality indices, including creepage, recoil, and radial spring back, which are influenced by the hemming process parameters and geometry design. Regression analysis was performed to determine the relationship between input parameters and output quality indices, providing valuable insights into the significance of the selected parameters. Takatsu and Aoki [6,7] investigated the dynamic strain hardening phenomenon and its microstructural changes in steel sheets during the hemming process. Their study demonstrated the macroscopic bending mechanism of steel sheets and the associated changes in microhardness and morphology, providing insights into the dynamic strain hardening phenomenon. Liu and Lin [8] developed a simulation model for the sheet metal hemming process. Based on the ASTM-E140 standard [9], they proposed a hardness-to-strain conversion formula. By comparing the simulated strain results at the hemmed sheet cross-section with the results from hardness-to-strain experiments, they investigated the material hardening behavior during the hemming process.

When it comes to studies on roller hemming processes, Yoon et al. [10] introduced a new and improved hemming process, namely roller hemming, which utilizes a roller guided by a robot along the hemming line, effectively bending the flanged height along the panel. Le Maoût and Thuillier [11] investigated the effects of geometry and pre-strain on roll-in, load, and damage occurrence by comparing classical and roll-hemming processes. Their findings also provided valuable insights for the optimization of the roller hemming process. Additionally, Selim [12] investigated the effect of using roller hemming replacements in conventional techniques in the automotive industry. Their numerical analysis could predict process outcomes and involved a comparison of five-element formulations, ultimately identifying the fully integrated formulation as the most effective method because the bending angle could influence wrinkling, hemming forces, and plastic strain. Hu and Lin [13] predicted the limits of roller hemming using a ductile fracture criterion. The authors conducted experimental analyses on aluminum alloy sheets, accounting for isotropic and kinematic hardening. A forming limit stress curve at fracture (FLSCF) was derived to evaluate fractures in roller hemming simulations. Serrated strain paths were observed, and the comparison between experimental and simulation fracture zones demonstrated the efficacy of FLSCF in predicting roller hemming fractures. Li and Hu [14] investigated the cyclic hardening behavior of roller hemming and found that strain hardening occurred, with no plastic deformation happening before the hemming process. Esquivel et al. [15] proposed an offline compensation method for the external forces on rollers to minimize their impact on the dimensional parameters of the roller hemming process and enhance the quality of the hemmed panel. Li et al. [16] proposed the incorporation of adhesive between the outer and inner panel, discussing its effects on the creepage and growing behavior during the roller hemming process. Huang and Jiang [17] proposed a vision-based, path-guidance method to achieve die-less roller hemming, enhancing both precision and automation in the process. Li and Zhu [18] investigated a smooth particle hydrodynamics (SPH)-FEM coupled model to simulate the behavior of viscous adhesive in roller hemming. Their study revealed that, compared to traditional roller hemming, the external force exerted on the roller increased, leading to improved quality in autobody closure panel manufacturing. Wang and Zhu [19] proposed a differential geometry-based method for solving the roller pose and trajectory, aimed at enhancing the quality and efficiency of precision hemming for curved panels. This approach provides valuable insights into improving the hemming process for complex geometries.

As mentioned above, only a limited number of research studies have investigated the mechanical relationship between roller and panel in the context of roller hemming. Therefore, in this study, our objective was to investigate the roller hemming process on both straight-edge and curved-edge sections. This work focuses on the external forces, thickness, and creepage/growing of the hemmed panel in both straight-edge and curved-

edge sections, analyzed through simulation and experimental methods. Particular emphasis is placed on hot-dip galvanized steel panels conforming to the SGCC grade of the JISG 3302 standard [20], which is widely used in automobile outer panels, analyzed through both simulation and experimental methods.

2. Simulation of Roller Hemming

2.1. Pre-Simulation Material Preparation

In this research, the SGCC grade of the JISG 3302 standard refers to an automobile hot-dip galvanized steel pane, whose chemical composition is shown in Table 1. To obtain the mechanical properties required for finite element model development, tensile tests were conducted on the material, as depicted in Figure 1a. The experimental conditions for the tensile test are presented in Table 2, including the parameters used to measure the tensile load, as well as the width and length of the specimen, under a tensile velocity of 300 mm/min as set on the tensile machine. Subsequently, based on the stress–strain relationship introduced by Arai and Masada, [21] these data were utilized in Equations (1) and (2) to derive the nominal stress–strain values. Next, Equations(1) and (2) were integrated into Equations (3) and (4) to obtain the true stress–strain results. Finally, the stress–strain curve relationship was plotted, as depicted in Figure 1b.

$$\sigma_n = \frac{P}{S_0} \tag{1}$$

$$\varepsilon_n = \frac{\Delta l}{l_0} \tag{2}$$

$$\sigma_t = \sigma_n(1 + \varepsilon_n) \tag{3}$$

$$\varepsilon_t = \ln(1 + \varepsilon_n) \tag{4}$$

σ_n: nominal stress [MPa]; P: tensile load [N]; S_0: specimen cross-sectional area [mm^2]; ε_n: nominal strain; Δl: elongation in the length direction [mm]; l_0: initial length [mm]; σ_t: true stress [MPa]; ε_t: true strain.

Table 1. Chemical composition of SGCC (wt%).

Material	Carbon	Mangenese	Phosphorus	Sulfur
SGCC	0.15	0.8	0.05	0.05

Table 2. Experimental conditions of tensile test.

Equipment	Material	Width [mm]	Length [mm]	Thickness [mm]	Tensile Velocity [mm/min]
Tensile testing machine	SGCC	25	50	0.75	300

The panel, made of hot-dip galvanized steel (the SGCC grade of JISG 3302), was subjected to tensile testing to determine its mechanical properties using a tensile testing machine (Figure 1a). As shown in Table 3, the panel sample was clamped onto the testing machine and subjected to increasing tensile force until failure. The machine recorded the applied force and the resulting deformation, allowing the calculation of key mechanical properties such as yield strength, tensile strength, modulus of elasticity, and Poisson's ratio.

Based on the tensile curve in Figure 1b, the material's mechanical behavior closely aligns with the isotropic hardening model. Therefore, this model was applied in the simulation to represent the material's behavior. The material deformed at room temperature with uniform forming speed, neglecting strain-rate effects. As shown in Figure 1b, in the

elastic region the material followed Hooke's law (Equation (5)), where σ_e represents the elastic stress (MPa), E denotes the modulus of elasticity (MPa), and ε is the strain. In the plastic region, it followed the Ludwik hardening model (Equation (6)), where σ_p is the plastic stress, σ_y is the yield strength, K is the hardening coefficient, ε_p is the plastic strain, and n is the hardening exponent, with the value n = 0.2 obtained by fitting the true stress–strain data [22].

$$\sigma_e = E \cdot \varepsilon \tag{5}$$

$$\sigma_p = \sigma_y + K \cdot \varepsilon_p^n \tag{6}$$

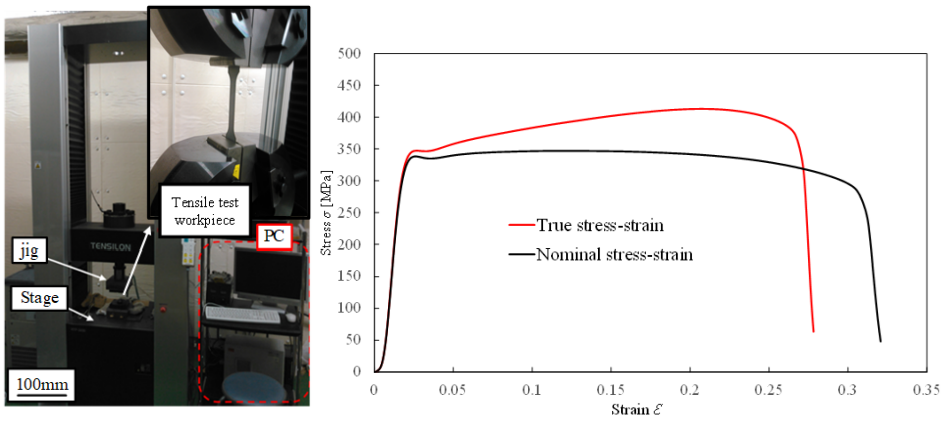

(**a**) (**b**)

Figure 1. Tensile testing machine was employed to obtain stress and strain data from a hot-dip galvanized steel panel (the SGCC grade of JISG 3302), offering valuable insights into the material's behavior under tension. Nominal stress–strain and true stress–strain data are represented by the black curved line and the red curved line, respectively. (**a**) A tensile testing machine. (**b**) The curve figure of strain-stress.

Table 3. Mechanical properties of SGCC.

Material	Yield Point [MPa]	Tensile Strength [MPa]	Elastic Modulus [GPa]	Poisson's Ration
SGCC	300	412.43	210	0.3

2.2. Establish Model of Simulation

Commercial finite element software, DEFORM ver. 11.0, for sheet metal forming was utilized to simulate the roller hemming process. Finite element analysis (FEM) was employed for two reasons. On the one hand, this approach can flexibly adjust the process parameters of the rolled edge and subsequently simulate and analyze rolled edge forming under different process parameters in a relatively short period, which increases its efficiency and saves time. Notably, this also eliminates the costly trial-and-error approach that is traditionally used for the quality debugging of rolled edges. On the other hand, finite element analysis reduces the labor and material consumption associated with this traditional process. The results of the FEM numerical analysis were utilized to optimize the geometric process parameters. Technical standards for roller hemming process parameters were established. This in turn ensured that high-quality results could be achieved more efficiently and at a reduced cost. True stress-true strain is solely relevant for uniform deformation. In the process of inputting material data into DEFORM, we define the range from the lower yield point to the tensile strength (maximum load point) as exhibiting uniform deformation. Subsequently, stress–strain data for this deformation are integrated into the DEFORM pre-processing material library, after the acquisition of the material properties from Figure 1b.

As shown in Table 4, the model used in DEFORM was employed to simulate the roller hemming process. The simulation encompassed both straight-edge and curved-edge flat surfaces, as these two parts are integral to both simulation and experimental setups. The entire model was created in a three-dimensional (3D) framework using the Lagrangian incremental method and a sparse solver to enhance computational efficiency. The Newton–Raphson iteration method was selected to ensure convergence of the calculation results. The roller and die were treated as rigid bodies, while the door panel was modeled as an elastic-plastic body using a tetrahedral element. The tetrahedral element compared to shell elements accounted for both node rotation and torsion. This allowed for a more accurate representation of the interaction forces and the deformation behavior of the entire door panel during the roller hemming process. The mesh grid size for the entire door panel area was set at 0.3 mm, resulting in a total of 200,000 finite elements. Considering the smoothness of both the panel and the roller surfaces, the roller was assumed to rotate frictionlessly along its axis of revolution. A shear friction coefficient and a normal Coulomb friction coefficient of 0.13 were applied between the panel, roller, and die [23]. The contact settings for the simulation process in both straight-edge and curved-edge were as follows: During the flange step, the die, panel, and holder were set to face contact, with no relative movement. In the pre-hemming and final-hemming steps, the roller was configured to rotate along its axis parallel to the length of the panel, while the panel maintained face contact with the die. Additionally, the non-deformed surface on the exterior of the panel was designated as a symmetric surface. The geometric parameters for the numerical model of the straight-edge and curved-edge, as well as the experimental setup for roller hemming on curved-edge flat surfaces, are presented in Figure 2. The roller diameter was set to 100 mm. For the curved-edge flat surface, the door panel exhibited a radius of curvature of 150 mm, with an arc length of 100 mm. The corresponding central angle of the door panel for this arc length was calculated to be 38.42°, as described in Equation (7), approximately corresponding to the position of the curved part (between P7 and P8) in the experimental setup, as illustrated in Figure 2a. For the straight-edge flat surface, the length of the door panel was set to 150 mm. The marker points along the actual straight portion of the panel were equally spaced (marked by P9–P14), as illustrated in Figure 2b. For the purpose of subsequent simulation and post-experimental comparison of the panel's cross-section profile, the samples were divided into three sections, S1, S2, and S3, in the curved-edge (experiment P7–P8 position in Figure 2a) of the simulation model and the experiments of the curved-edge section, and the samples were divided into three sections, W1, W2, and W3, in the simulation model of the straight-edge.

$$\theta = \frac{l \times 360}{2 \times \pi \cdot r} = \frac{100 \times 360}{2 \times 3.14 \times 150} \approx 38.42^{\circ} \quad (7)$$

Table 4. Simulation of the roller hemming process by DEFORM.

Simulation Model Properties	Context
Simulation model position	straight-edge flat surface curved-edge flat surface
Simulation model type	three-dimensional
Object type	roller and die setting as a rigid body door panel setting as elastic-plastic body
Type and number of meshing settings	tetrahedral element 200,000
Roller diameter	100 mm
Roller speed	100 mm/s
Calculation type	lagrangian incremental
Calculation solver	sparse
Iteration method	Newton–Raphson
Friction coefficient	panel and die: 0.13 roller and panel: 0.13

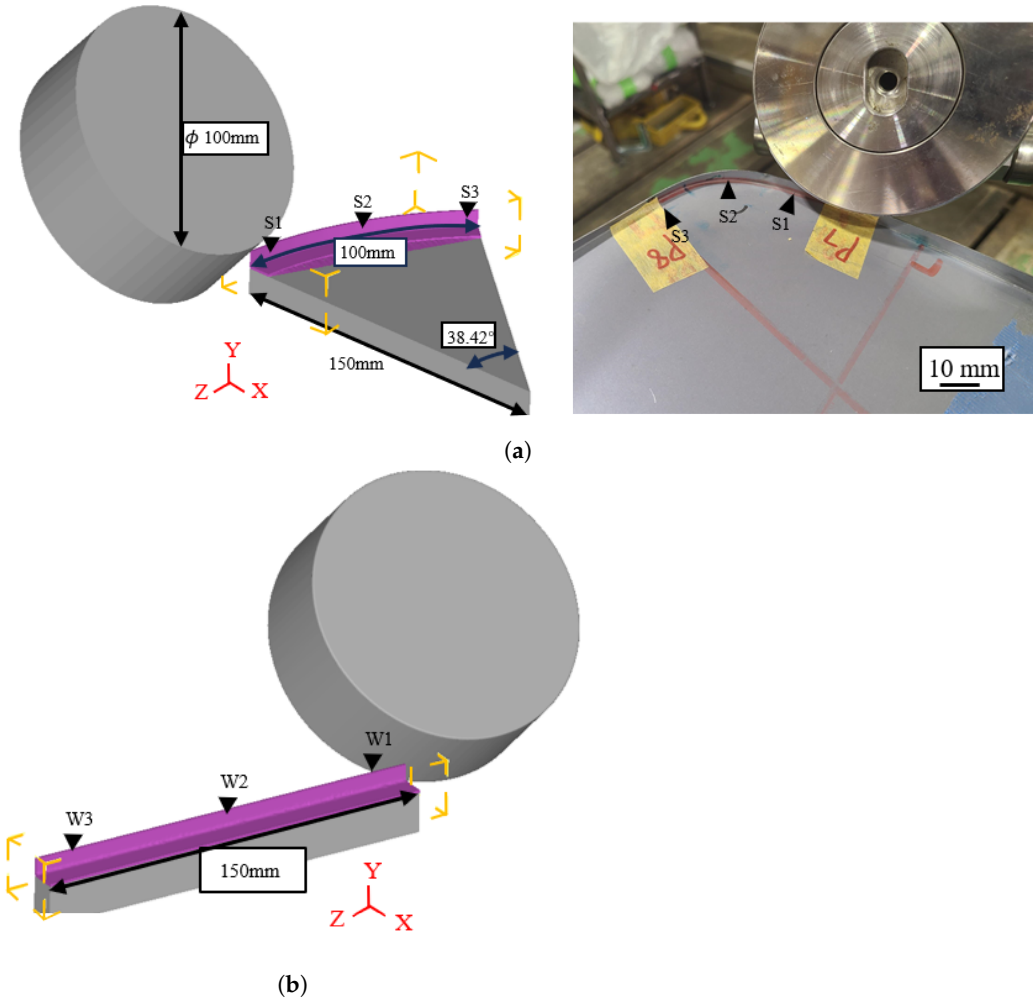

Figure 2. Simulation model and experimental process of roller hemming constructed in curved-edge sections (S1 to S3) and simulation model of straight-edge sections (W1 to W3). The straight-edge sections had approximately 70 mm of spare space, while the curved-edge sections had approximately 45 mm of spare space. (**a**) Numerical model and experimental setting of flanging at 90° in the curved-edge part. (**b**) Numerical model of flanging at 90° in the straight edge.

2.3. Results of Simulation

The DEFORM simulation process involves setting geometry relationships with roller hemming objects, controlling simulation parameters, inputting materials, meshing settings, defining friction coefficients, specifying roller movement, setting boundary conditions, and running the simulation. These operations were conducted to generate the stress distribution for the roller in both the straight-edge and curved-edge sections; the maximum value of stress during pre-hemming (458 MPa and 441 MPa, respectively) and final hemming (491 MPa and 500 MPa, respectively) were observed. Moreover, it was found that there was a uniform deformation in the width direction. The main deformation area is in the vicinity of the bending center in the section view. The stress distribution indicates a higher overall stress level in the curved-edge section compared to the straight-edge section, exhibiting greater deformation in the former, as shown in Figure 3.

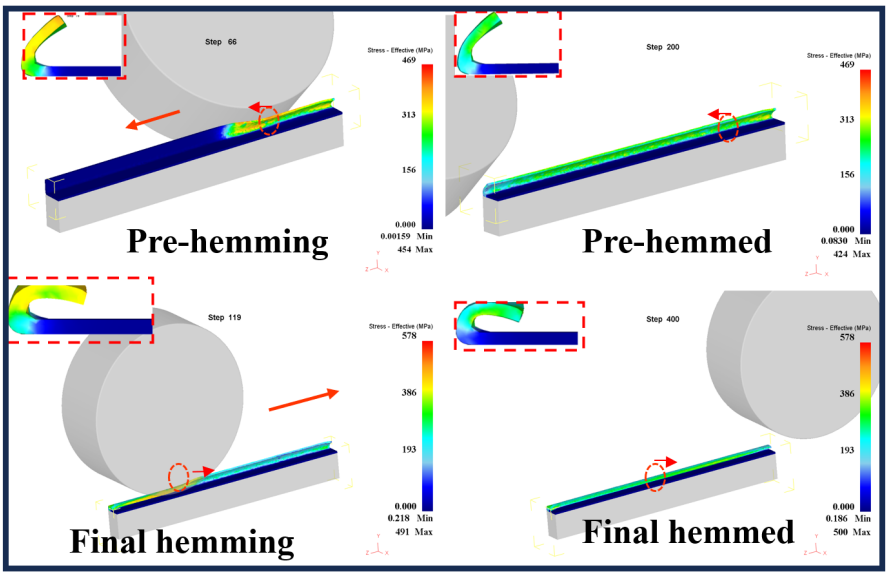

(**a**)

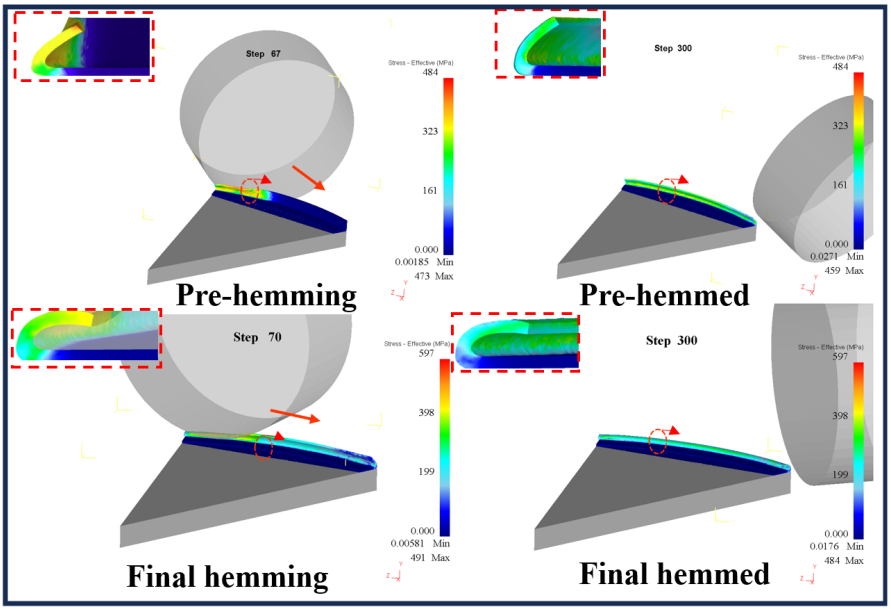

(**b**)

Figure 3. Simulation results of the roller hemming process demonstrating the stress-effective distribution of the curved- and straight-edge flat surface of the roller hemming process from pre-hemming at 45° and final hemming. (**a**) Straight-edge part. (**b**) Curved-edge part.

Figure 4 shows the numerical outcomes of the external forces exerted by the roller on both the curved-edge and straight-edge parts during the pre-hemming at 45° and the final hemming. In the roller hemming process, where the rollers were set as rigid bodies, the reaction forces acting on the rollers during the pre-hemming process were measured using a reference point on the rollers. The magnitude of this force serves as an indication of the force exerted on the panel. Then, the maximum normal force on the roller reaches approximately 1508 N and the maximum tangential force reaches 317 N during the pre-hemming stage in the straight-edge section. In the final-hemming stage of the straight-edge section, the maximum normal force increases to about 2090 N, and the maximum tangential force to 279 N. In the curved-edge section during the final-hemming stage, the maximum normal force on the roller reaches approximately 1725 N and the maximum tangential force reaches 280 N, while in the pre-hemming stage the maximum

normal force reaches about 1484 N and the maximum tangential force is 471 N. Notably, the external force values in the smooth stage exhibit greater fluctuations in the curved part compared to the straight part, particularly in terms of normal force. The tangential force in both the pre-hemming and final-hemming stages shows minimal differences between the straight-edge and curved-edge sections, with values generally around one-fifth of the normal force.

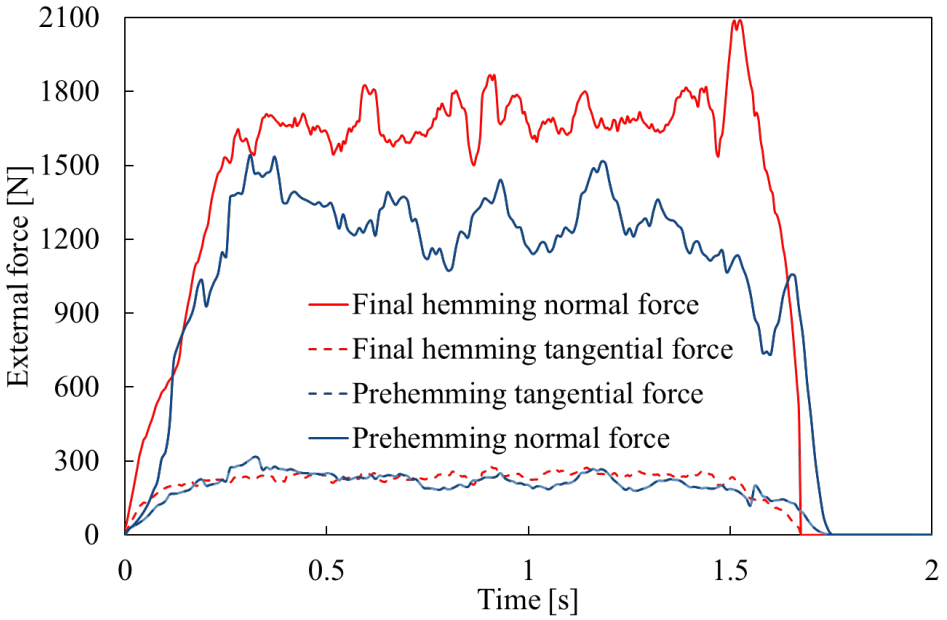

(**a**)

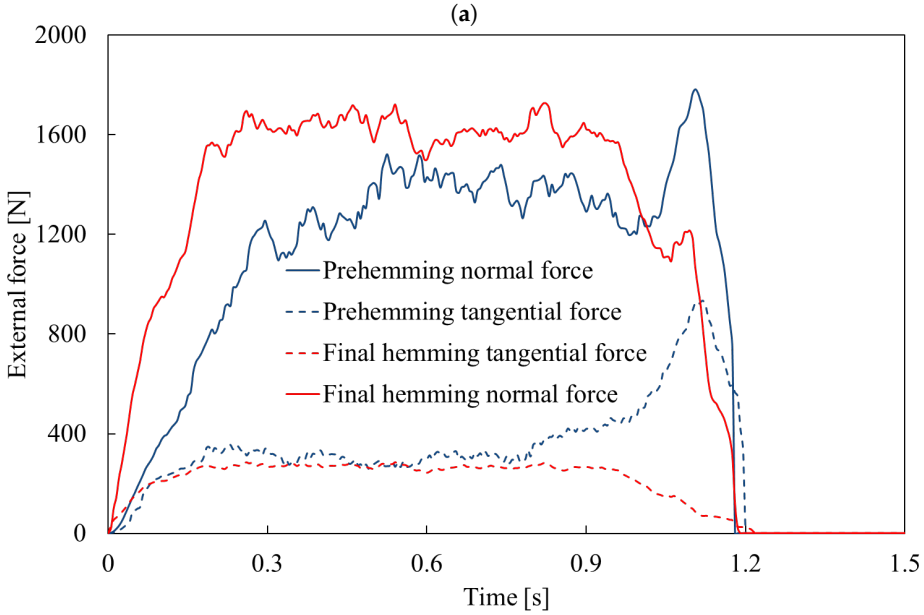

(**b**)

Figure 4. The numerical results of the external forces (tangential force, representing the force in the x direction, and normal force, representing the force in the y direction, as depicted in Figure 5b, Load Measurement Tool Model) in the roller hemming process. (**a**) Straight-edge part. (**b**) Curved-edge part.

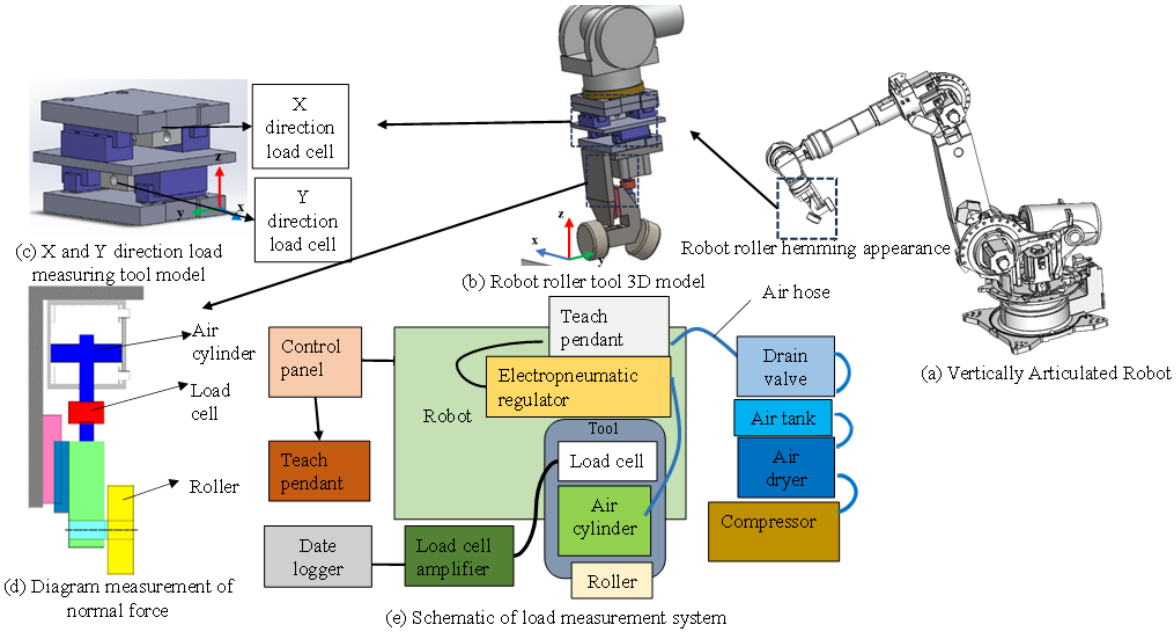

Figure 5. Schematic of the roller hemming experiments system. (**a**) Vertically articulated robot. (**b**) Robot roller hemming tool. (**c**) External force measuring tool model in the tangential direction. (**d**) Measurement of normal force device. (**e**) Schematic diagram of the load measurement system.

3. Roller Hemming in an Experimental Case

3.1. Experiments of Load Cell Calibration

The experimental process was carried out using a robotic system, specifically an industrial robotic arm, as illustrated in Figure 5a, which presents a 3D model of the industrial robot arm that had the same structure and functions as those of the actual experimental equipment. In this study, a tool attached to the tip of the robot rollers was employed to accomplish the robot roller hemming process. The robot used in the present study was operated along six axes of rotation; an additional device was attached to the conventional tool (load measurement system) to measure loads in three directions, and the roller rotation moved along the vertical direction z (red arrow) and tangent direction x (blue arrow). The sensor was installed at the end of the robot arm, as shown in Figure 5b, and the device structure is illustrated in Figure 5c, which illustrates a model of the tool used for measuring tangential direction external forces, while Figure 5d depicts a schematic diagram of the device for sensing normal direction external forces on the roller, positioned on the robot arm. The complete acquisition of external forces during the roller hemming process is displayed in Figure 5e, where the device captures real-time sensing signals, which are subsequently computer-converted from voltage to load data. Specifically, the electrical signal is obtained from the load cell (PUSHTON PSD-S1), then amplified by the load cell amplifier (CALT DY510), and finally output to the data logger (HIOKI LR8431). The data logger comes with built-in software that exports the data in CSV format for further analysis on a computer. In this study, three channels were used with a sampling rate of 100 times per second.

Figure 6 illustrates a schematic diagram of load calibration, where the load output from the universal material testing machine is converted into voltage. Load Cell X measures the load in the direction of roller travel, while Load Cell Y measures the load perpendicular to the roller travel direction. Calibration for each load condition (50 kgf, 100 kgf, 150 kgf, and 200 kgf) was conducted three times, and the average value was utilized as the calibration value, representing the load per 1 V.

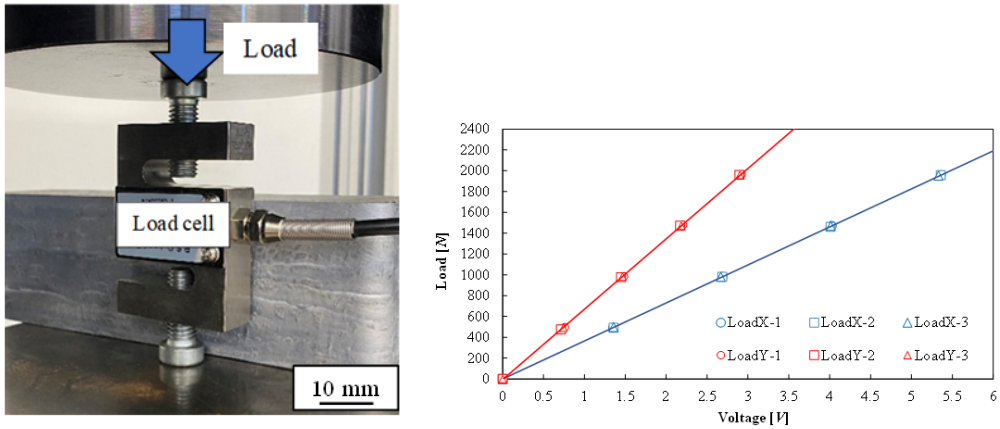

(**a**) (**b**)

Figure 6. Calibration experiment of the load cell involved applying external forces installed in the robot arm in Figure 5b during the roller hemming process; the resultant curve illustrates the conversion from voltage to load in both the X and Y directions. (**a**) Diagram of load cell (PUSHTON PSD-S1) calibration test. (**b**) Load and voltage obtained by compression.

Based on the data shown in Figure 6b, the following Equation (5) obtained Equations (6) and (7). In this section, the results for Load Cell X and Load Cell Y are depicted in Figure 5c. Load Cell X registered a measurement of 669.51 N per 1 V, while Load Cell Y recorded 365.38 N per 1 V.

$$A = F / V_{Lc} \tag{8}$$

A: Load per 1V [N/V]; F: Load [N], measured by tensile/compression tester; V_{Lc}: Voltage [V], measured by data logger.

$$F_{LcX}[N] = 669.51 \left[\frac{N}{V}\right] \times V_{LcX}[V] \tag{9}$$

$$F_{LcY}[N] = 365.38 \left[\frac{N}{V}\right] \times V_{LcY}[V] \tag{10}$$

The experimental conditions for both the tensile and compression testing machines, as well as load calibration details, are presented in Table 5. Figure 6a depicts the experimental setup, illustrating the relationship between the tensile/compression testing machine and the associated tools. The load and voltage values were recorded for each stroke during the first and second measurements under different set pressures. Calibration experiments on the Z direction load cell for measuring the normal external load on the rollers were conducted using a tensile/compression testing machine. The machine operated at a speed of 0.1 mm/min, with a travel distance of 1.1 mm. Air pressure, regulated by an air regulator, was set at 0.05 MPa, 0.10 MPa, and 0.20 MPa for each measurement, with each setting tested twice. The experimental results of voltage conversion loads are shown in Figure 7. Readings were taken at 20 points between 0 mm and 1 mm, with 0.05 mm intervals to determine the load per V (N/V). The load-to-voltage ratio was calculated for each load cell, resulting in an average load per 1V of 210 N/V after two measurements for set pressures of 0.05 MPa, 0.10 MPa, and 0.20 MPa. Table 6 presents the load per voltage (V) values obtained from the two measurements for each set pressure condition.

Table 5. Experimental conditions of Z direction load cell in the robot arm's coordinate system, as shown in Figure 5b.

Test Speed	0.1 [mm/min]
Amount of movement	1.1 [mm]
Maximum load	2500 [N]
Air pressure	0.05 [MPa], 0.10 [MPa], 0.20 [MPa]

Table 6. Calibration experimental results for Z direction load cell in the robot arm's coordinate system, as shown in Figure 5b.

Air Pressure in Cylinder [MPa]	Test 1 [N/V]	Test 2 [N/V]
0.05	221.4473	219.6515
0.10	205.8303	208.9549
0.20	205.0219	203.5119
Measurement average [N/V]	210.7363	

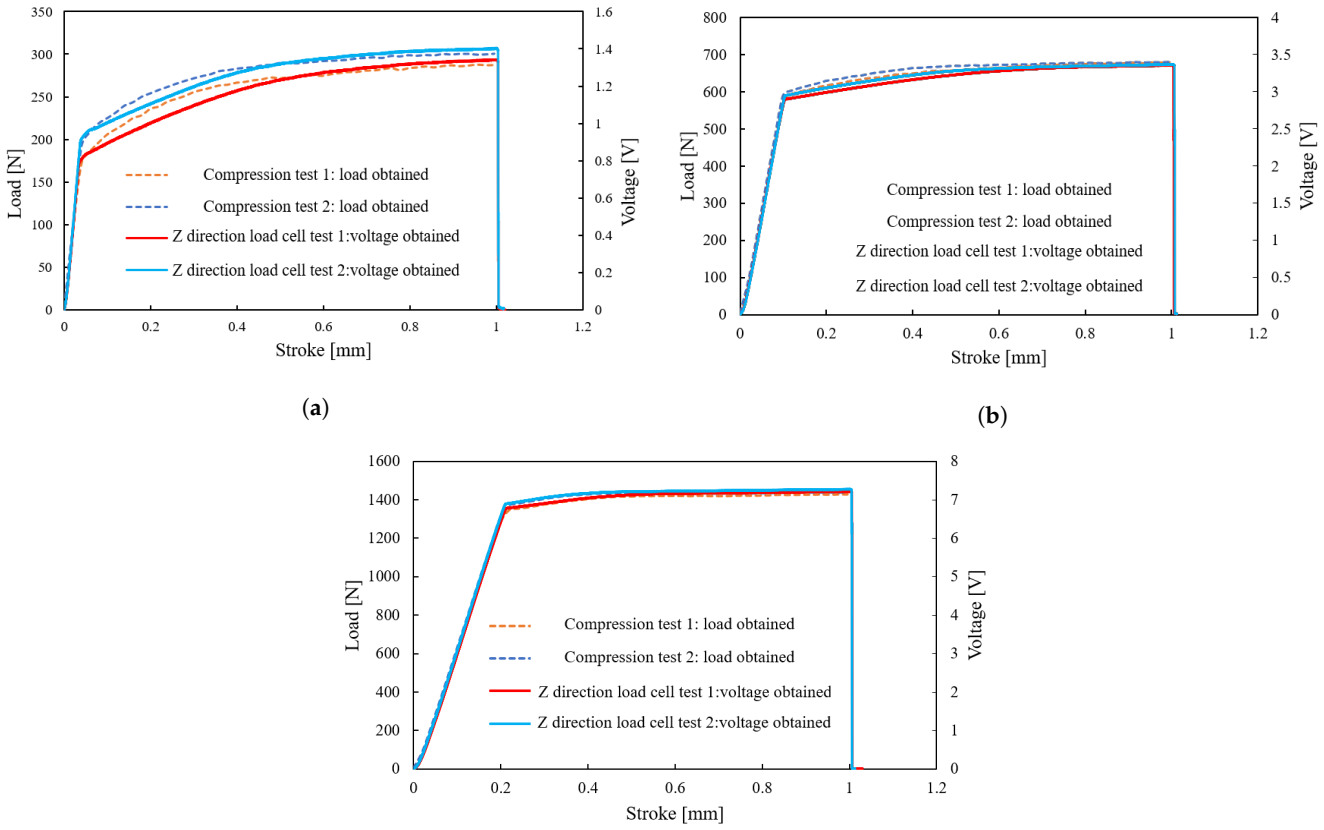

Figure 7. The calibration experiment of the load cell involved applying external forces during the roller hemming process, and the resultant curve illustrates the conversion from voltage to load in the Z direction of the robot's coordinate system, as shown in Figure 5b, under air pressures of 0.05 MPa, 0.10 MPa, and 0.20 MPa, respectively. (**a**) 0.05 [MPa] air pressure. (**b**) 0.10 [MPa] air pressure. (**c**) 0.20 [MPa] air pressure.

3.2. Experiment of Roller Hemming

The experimental equipment used in this study includes an industrial robot (YASKAWA-ES165D, YASKAWA Co., Ltd., Fukuoka, Japan), a load cell (PUSHTON PSD-S1, Walfront Co., Ltd., Shenzhen, China), a load cell amplifier (CALT DY510, CALT Co., Ltd., Shanghai, China), a data logger (HIOKI LR8431, HIOKI Co., Ltd., Nagano, Japan), a roller, and a platform, as shown in Figure 5. During the roller hemming process, the load cell was mounted on the robotic arm, as indicated in Figure 5c, and the robot's built-in sensors, as shown in Figure 5d, were also employed. The real-time data from the sensing signals were captured by the data logger, which converted the signals and output them to a computer. This setup allowed simultaneous monitoring of forces in three directions. The experiments were then conducted in accordance with the roller's path, as illustrated in Figure 8. The door panel, previously flanged to 90°, initiated roller machining directly from position P1 to position P14 and subsequently the pre-hemming process at a 45° angle. Immediately after the final-hemming process, the roller returned to P1 and again moved back to P14, thereby completing the entire robot rolling hemming process. This process encompassed flanging to 90°, pre-hemming at 45°, and final hemming. The specific geometric parameters of the experimental setup are detailed in Figure 9. The inner and outer panel thicknesses (t_1 and t_2) were both 1 mm; however, the tensile test specimens were made from JISG 3302 SGCC hot-dip galvanized steel with a thickness of 0.75 mm. The difference in thickness between the tensile test specimens and the door panels was not expected to have a significant impact on the resulting stress–strain behavior. The flanging radius, R, was 1 mm; the flanging height, F, was 7 mm; and the distance between the inner and outer panels, G, was 2 mm. The roller diameter, $\boldsymbol{\phi}$, was 100 mm, and the roller's speed was set to 100 mm/s. The external force data at positions P1 to P14 were obtained after the roller hemming experiment. Following the final-hemming stage, the creepage/growth values at the curved-edge positions S1, S2, and S3 (as shown in Figure 2a), as well as at the straight-edge positions P10, P12, and P14, were measured using a vernier caliper.

As shown in Figure 10, the experimental results illustrated the external forces applied by the roller on both curved-edge (P7–P8) and straight-edge (P9–P14) parts. Through the application of Equations (6) and (7), as well as the data presented in Table 6, the voltage data collected from the load cell is converted into the corresponding external force exerted on the roller. The load measurement tool model presented the components of the external forces in the x, y, and z directions, where the voltage signals were acquired from the force sensor and subsequently transformed into corresponding external force values. In the experimental results of the straight-edge part, both the external tangential and normal forces during the pre-hemming stage were smaller than those during the final-hemming stage. However, during the pre-hemming stage, the data for the external tangential and normal forces exhibited some degree of noise, possibly due to the rigidity of the robot arm itself. In the curved-edge part, the external force exerted by the roller in the direction of travel caused the material fibers to pile up, resulting in significant noise during both the pre-hemming and final-hemming stages.

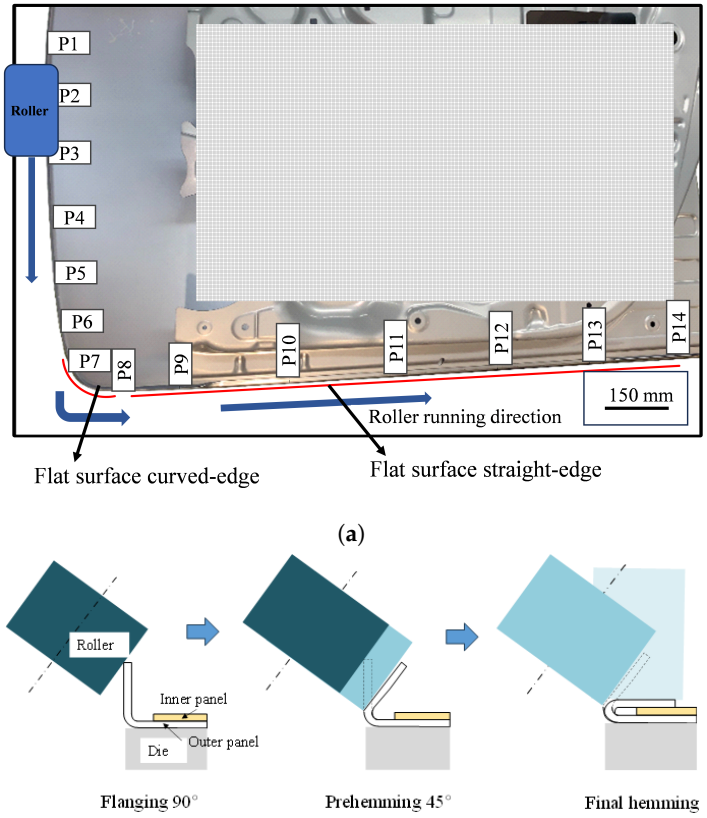

Figure 8. Schematic of roller running path and roller hemming process: flanging at 90°, pre-hemming 45°, and final-hemming stages in a flat surface curved and straight-edge (from P1 to P14). (**a**) A full view of the experimental process of car door roller hemming. (**b**) Roller hemming experiments were conducted following three stages.

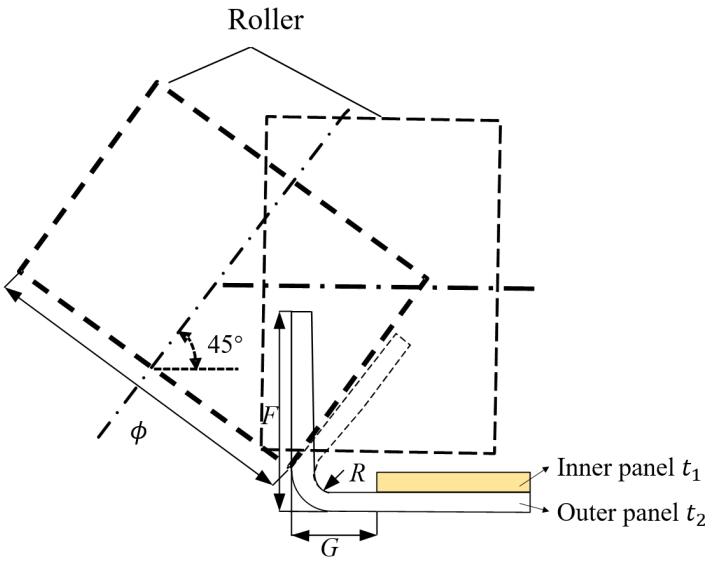

Figure 9. Schematic of the straight-edge flat surface and curve-edge flat surface geometry. Both inner and outer panel thicknesses, t_1 and t_2, respectively, were 1 mm; flanging radius, R, was 1 mm; flanging height, F, was 7 mm; the distance between the panels was 2 mm; and the roller diameter, $\boldsymbol{\phi}$, was 100 mm.

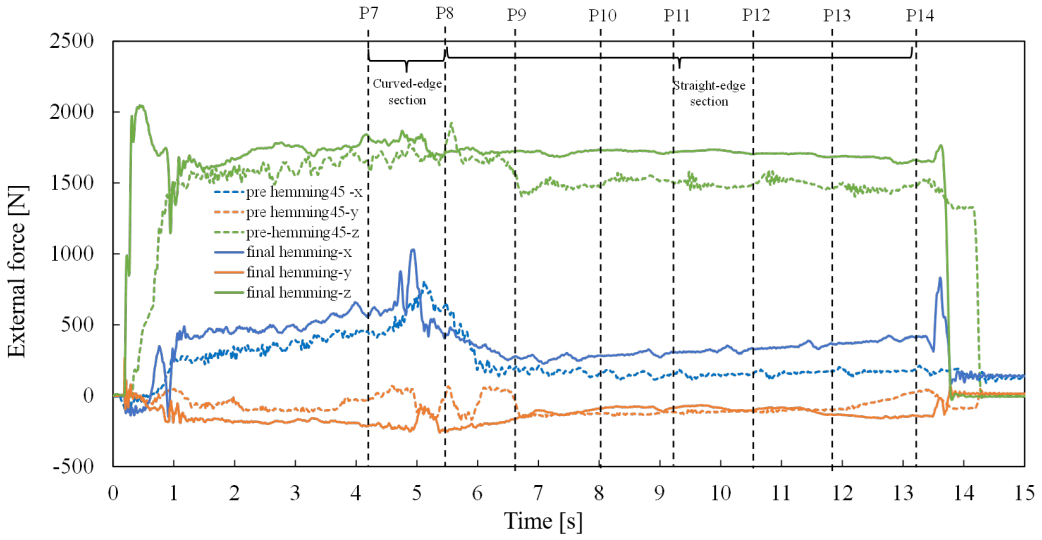

Figure 10. Experimental results involved measurements of the external forces in the x, y, and z directions, as shown in Figure 5b during the pre-hemming at 45° and final-hemming stages of roller hemming conducted in both curved-edge and straight-edge sections.

4. Comparison of Simulation and Experiment Results

The simulations and experimental analyses primarily focused on the external forces in the X and Z directions. The external force in the X direction was identified as the tangential force, while the external force in the Z direction was referred to as the nominal force. As Figure 11 shows, in both the curved-edge and straight-edge experimental parts the average values were obtained by analyzing the data from positions P7 to P8 and from positions P9 to P14 on the door panel, respectively, as depicted in Figure 8a. For simulation results, stable external force regions were identified to exclude the rapid fluctuations observed in the initial rapid increase and end rapid decrease curves depicted in Figure 4, ensuring the calculation of reliable average values. The average values of the obtained tangential external forces during pre-hemming at 45° and final hemming were 225 N and 239 N (straight-edge section) and 257 N and 262 N (curved-edge section), respectively. The corresponding average values of the obtained normal external forces were 1280 N and 1704 N (straight-edge section) and 1345 N and 1610 N (curved-edge section), respectively. The experimental results confirmed the simulation findings, with the measured average values of external tangential forces being 565 N and 574 N (curved-edge section) and 176 N and 223 N (straight-edge section) for pre-hemming 45° and final hemming, respectively. Similarly, the measured average values of external normal forces were 1705 N and 1764 N (curved-edge section) and 1468 N and 1705 N (straight-edge section) for pre-hemming at 45° and final hemming, respectively.

Compared to the corresponding simulated values, the experimental measurements consistently showed higher normal forces in both the straight- and curved-edge sections. Tangential force values were also higher in the straight-edge section. Additionally, the normal external forces consistently exceeded the tangential forces. In the curved-edge section, both simulation and experimental results indicated that the roller hemming process leads to a pile-up phenomenon, where material accumulates along the edges due to the transverse slip of the door panel material. This accumulation affected the final shape and quality of the panel. As shown in Figure 11, the tangential force on the curved-edge was greater than that on the straight-edge, likely due to the more complex stress state in the curved area caused by material fiber accumulation during deformation. The large discrepancy between the experimental and the numerical results, particularly in the curved-edge section, may also stem from differences in boundary conditions and friction coefficients between the simulation and experiments, as well as the unaccounted influence of the robotic arm's rigidity during the hemming process.

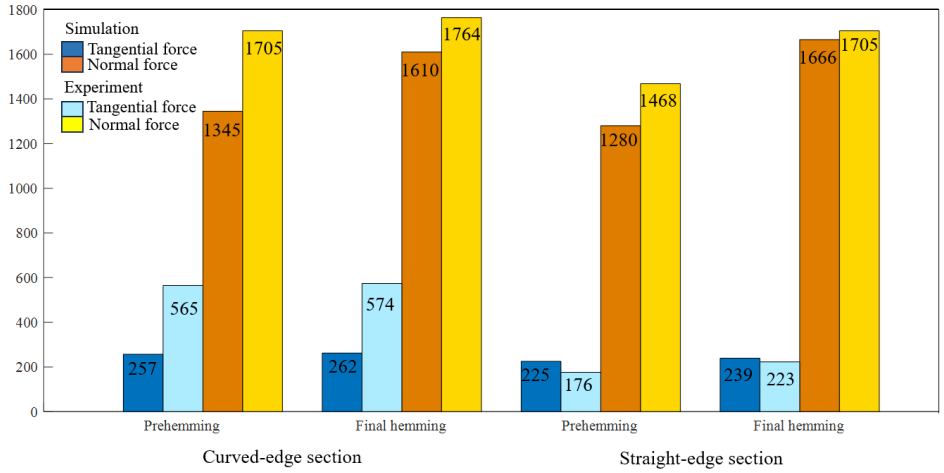

Figure 11. Comparison of the mean values of external forces (tangential force represents the force in the x direction, while normal force represents the force in the y direction, as depicted in Figure 10, Load Measurement Tool Model) in roller hemming.

The outer end of the panel to the inside of the reference line was defined as "creepage", with negative values indicating movement inwards. It was desirable that the values of both growing and creepage are as small as possible. The comparison between the experimental and the simulation results revealed creepage or growth; the initial flanging at the 90° position of the panel before bending deformation was defined as the reference line. The outer end of the panel to the left of the reference line was defined as "growing", with positive values indicating growth in that direction, as shown in Figure 12. Simulation and experimental results demonstrate that the panel thickness, H, except for Figure 13b, exhibits an initial increase followed by a decrease, with the maximum thickness occurring at the midpoint in both the straight-edge and curved-edge sections, as depicted in Figure 13. In the experiment, we measured the outer profile three times at every marked position. Additionally, in both the straight-edge and curved-edge sections, simulation result of the door panel's cross-sectional shape revealed that the simulation consistently depicted the panel's thickness after bending to be approximately 0.4 mm and 0.2 mm, respectively, larger than the experimental results.

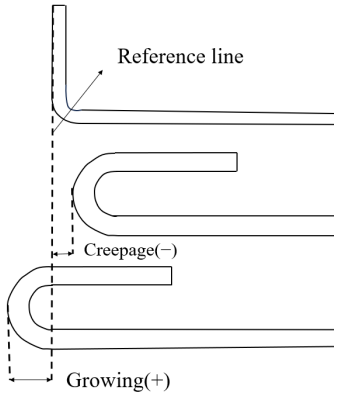

Figure 12. Displacement on the roller hemming reference line showing creepage and growing.

The reference line represents the initial flanging position of the panel before any bending deformation occurred, as shown in Figure 14. Therefore, it was essential to minimize both of these values (growing and creepage) to obtain optimal results. Cross-sectional observations were made on the door panel, focusing on the outer profile of the outer panel, as shown in Figure 2. In the straight-edge section of the experiment, marked from P9 to P14 in Figure 8, points P10, P12, and P14 were selected, along with the straight-edge section of the simulation, marked as W1, W2, and W3, for cross-sectional

analysis. In the curved-edge section of the experiment, marked from P7 to P8 in Figure 8b, and in the curved-edge section of the simulation, points S1, S2, and S3 were selected for the cross-sectional analysis. More particularly, the experimental findings revealed that greater creepage was observed in the curved-edge part compared to the simulation results. This discrepancy in the geometric relationship between the finite element modeling of the curved part and the actual roller may lead to deviations from the simulation preset trajectory during travel. However, in both the curved- and straight-edge sections, the simulations indicated initial growth in the straight-edge and creepage in the curved-edge, whereas the experimental results exhibited creepage in both sections. This discrepancy can be attributed to the presence of a free edge in the initial position of both curved and straight edges during roller hemming in simulation operations. This discrepancy is further summarized in Table 7.

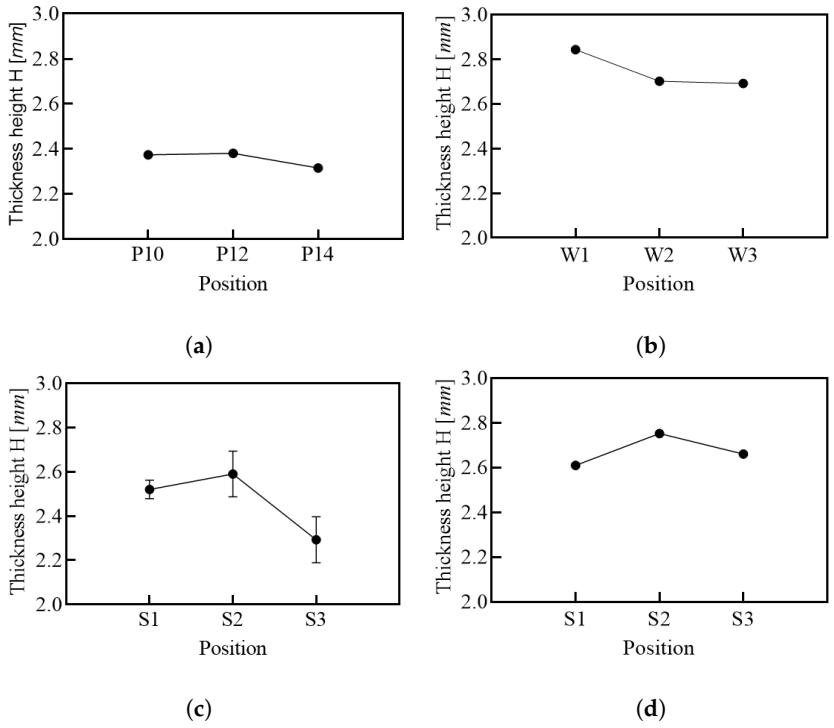

Figure 13. The panel thickness results obtained from both simulation and experimental roller hemming processes. In the straight-edge section, data were collected from positions P10, P12, and P14 during experimentation, and from positions S1, S2, and S3 during simulation. Similarly, in the curved-edge flat surface section, data were gathered from positions S1 to S3. Each position had approximately 50 mm of spare space in both simulation and experimentation. (**a**) Straight-edge experiment height. (**b**) Straight-edge numerical height. (**c**) Curved-edge experiment height. (**d**) Curved-edge numerical height.

Table 7. Comparison of creepage and growth values in the roller hemming process between our experiment and simulation.

	Measuring Position		**Creepage (−)/Growing Value (+) [mm]**		**Error [mm]**
	Experiment Position	**Simulation Position**	**Experiment Value**	**Simulation Value**	
Curved-edge part	S1	S1	−1.14	−0.2	0.94
	S2	S2	−0.94	−0.31	0.64
	S3	S3	−1.18	−0.48	0.7
Straight-edge part	P10	W1	−0.44	+1.44	1.88
	P12	W2	−0.45	+0.12	0.57
	P14	W3	−0.21	+0.12	0.33

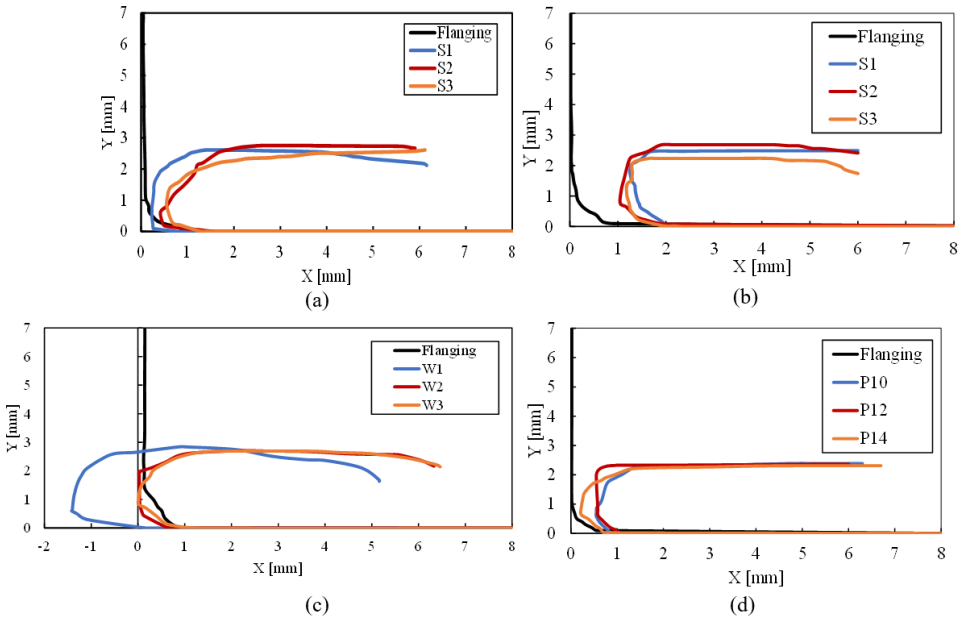

Figure 14. Displacement on the roller hemming reference line showing creepage and growing. (**a**) Numerical shape profile of curved-edge. (**b**) Experimental shape profile of curved-edge. (**c**) Numerical shape profile of straight-edge. (**d**) Experimental shape profile of straight-edge.

5. Conclusions

In this study, we conducted roller hemming experiments and simulations on straight-edge and curved-edge flat surfaces using a hot-dip galvanized steel panel (SGCC grade, JISG 3302). A finite element simulation model was established using DEFORM, and the external forces acting on the roller during the hemming process were quantified through comparison with experimental results. Our findings highlight the differences in stress distribution and deformation between the straight-edge and curved-edge sections. The results provide valuable reference data for future parameter optimization in the roller hemming process. Notably, stress concentrations were observed at the bending areas, with higher stress values in the final-hemming stage compared to pre-hemming, especially in the curved-edge section. These trends align with the observations of S. Thuillier et al. [11], further confirming the accuracy of our approach.

Our experimental and simulation results have significant implications for both the practical application and academic study of the roller hemming process. Detailed analysis of stress distribution and deformation behavior across different edge sections provides crucial insights into panel performance during the roller hemming process. Furthermore, the experimental measurements of external forces exceeded the simulated values in the normal direction for both the straight-edge and curved-edge sections, in addition to the tangential direction for the straight-edge section, highlighting the necessity for tailored processing guidelines specific to each panel section. These results are consistent with the studies of S. Thuillier et al. [11] and Hu et al. [15], which demonstrated that both the pre-hemming and hemming stages have minimal impact on growth, except near the free edge.

Despite the valuable contributions of this research, certain limitations should be addressed in future studies. First, the exclusion of data from the W1 position due to initial roller contact deviation indicates that further refinement in the experimental setup is necessary to capture a more accurate representation of the roller hemming mechanism. Additionally, the simulations indicated a consistent overestimation of panel thickness post-hemming compared to experimental results, suggesting that the current simulation model can be improved by incorporating more precise material behavior and boundary conditions. Future research should also explore the impact of additional parameters, such

as roller speed, panel material properties, and robotic arm dynamics, to further optimize the roller hemming process and improve overall manufacturing accuracy.

Author Contributions: Conceptualization, C.L. and W.L.; methodology, C.L. and W.L.; software, C.L.; validation, C.L.; formal analysis, C.L.; investigation, C.L.; resources, C.L. and W.L.; data curation, C.L. and W.L.; writing—original draft preparation, C.L.; writing—review and editing, C.L. and W.L.; visualization, C.L.; supervision, W.L.; project administration, W.L.; funding acquisition, W.L. All authors have read and agreed to the published version of the manuscript.

Funding: This research received no external funding.

Institutional Review Board Statement: Not applicable.

Informed Consent Statement: Not applicable.

Data Availability Statement: The original contributions presented in the study are included in the article; further inquiries can be directed to the corresponding author.

Acknowledgments: The authors would like to express their sincere gratitude to Yoshihiro Aoki and Shinichi Takatsu of Takatsu Co., Ltd. for their great support and advice. We would also like to thank Shinichi Nishida of Gunma University for his great advice and support regarding our simulations. Finally, the authors would like to express their gratitude to Akihiro TANAKA for his excellent contribution to experimental and simulation processes. The authors are grateful to the editors and the anonymous reviewers for their insightful comments and suggestions.

Conflicts of Interest: The authors declare no conflicts of interest.

References

1. MaoûT, N.L.; Manach, P.Y.; Thuillier, S. Influence of prestrain on the numerical simulation of the roller hemming process. *J. Mater. Process. Technol.* **2012**, *212*, 450–457. [CrossRef]
2. Hishida, Y.; Sato, Y. Analysis of hemming processes by the finite element method for improving hemming quality. In Proceedings of the 14th Biennial Congress of IDDRG, Munich, Germany, 21–23 April 1986; pp. 21–23.
3. Livatyali, H.; Larris, S. Experimental investigation on forming defects in flat surface–convex edge hemming: Roll, recoil and warp. *J. Mater. Process. Technol.* **2004**, *153*, 913–919. [CrossRef]
4. Zhang, E.; Wu, X.; Hu, S.J. A study on fundamental mechanisms of warp and recoil in hemming. In Proceedings of the ASME International Mechanical Engineering Congress and Exposition. American Society of Mechanical Engineers, Orlando, FL, USA, 5–10 November 2000; Volume 19166, pp. 563–569. [CrossRef]
5. Zhang, G.; Hao, H.; Wu, X.; Hu, S.J.; Harper, K.; Faitel, W. An experimental investigation of curved surface-straight edge hemming. *J. Manuf. Process.* **2000**, *2*, 241–246. [CrossRef]
6. Takatsu, S.i.; Aoki, Y.; Komoto, T.; Kumehara, H.; Lin, W. Further study on strain hardening of a steel panel in the hemming process. *Adv. Mater. Process. Technol.* **2022**, *9*, 1183–1198. [CrossRef]
7. Takatsu, S.i.; Aoki, Y.; Nitta, Y.; Komoto, T.; Kumehara, H.; Lin, W. Experimental study on strain hardening of steel panels in the hemming process. *Adv. Mater. Process. Technol.* **2021**, *8*, 2069–2086. [CrossRef]
8. Liu, C.; Iwasaki, A.; Lin, W. A fundamental study on the hardness-strain in bent cross-section of thin steel panels during the hemming process with a comparison between experimental and numerical approach. *Mech. Eng. J.* **2024**, *11*, 23–00256. [CrossRef]
9. *ASTM E140-19*; Standard Hardness Conversion Tables for Metals. ASTM International: Conshohocken, PA, USA, 2013.
10. Yoon, Y.; Shin, D.; Kim, D.; Kwak, H.; Ryu, Y.; Han, B. The study of roller hemming process for aluminum alloy via finite element analysis and experimental investigations. In *Technical Report*; SAE Technical Paper: New York, NY, USA, 2007. [CrossRef]
11. Le Maoût, N.; Thuillier, S.; Manach, P. Classical and roll-hemming processes of pre-strained metallic sheets. *Exp. Mech.* **2010**, *50*, 1087–1097. [CrossRef]
12. Gürgen, S. A parametric investigation of roller hemming operation on a curved edge part. *Arch. Civ. Mech. Eng.* **2019**, *19*, 11–19. [CrossRef]
13. Hu, X.; Lin, Z.; Li, S.; Zhao, Y. Fracture limit prediction for roller hemming of aluminum alloy sheet. *Mater. Des.* **2010**, *31*, 1410–1416. [CrossRef]
14. Li, S.; Hu, X.; Zhao, Y.; Lin, Z.; Xu, N. Cyclic hardening behavior of roller hemming in the case of aluminum alloy sheets. *Mater. Des.* **2011**, *32*, 2308–2316. [CrossRef]
15. Esquivel, E.; Carbone, G.; Ceccarelli, M.; Jáuregui, J.C. A dynamic compensation for roll hemming process. *IEEE Access* **2018**, *6*, 18264–18275. [CrossRef]
16. Li, J.; Zhu, W. Numerical simulation of the roller hemming process based on pressure-viscosity effect. *Int. J. Adv. Manuf. Technol.* **2019**, *105*, 1023–1039. [CrossRef]

17. Huang, Y.P.; Jiang, B.T.; Wu, C.H.; Chang, J.Y. Vision-Based Path Guidance to Achieve Dies-Free Roller Hemming Process. *Appl. Sci.* **2021**, *11*, 5741. [CrossRef]
18. Li, J.; Zhu, W.; Wang, S. Numerical quantification model and experiment of external force on roller hemming of curved edge aluminium alloy with adhesive. *Chin. J. Mech. Eng.* **2022**, *35*, 17. [CrossRef]
19. Wang, S.; Zhu, W.; Li, M. Differential geometry modeling and application of roller pose and trajectory of robot roller hemming for complex curved surface-curved edge panels. *Robot.-Comput.-Integr. Manuf.* **2023**, *83*, 102565. [CrossRef]
20. *JIS G 3302*; Hot-Dip Zinc-Coated Steel Sheet and Strip. Japanese Industrial Standards Committee: Tokyo, Japan, 2019.
21. Arai, M. No.1 Stress and Strain. *J. Jpn. Soc. Mech. Eng.* **2019**. Available online: https://www.jsme.or.jp/kaisi/1202-36/ (accessed on 13 October 2024).
22. Hill, R. *The Mathematical Theory of Plasticity*; Oxford University Press: Oxford, UK, 1950.
23. Thuillier, S.; Le Maoût, N.; Manach, P.Y.; Debois, D. Numerical simulation of the roll hemming process. *J. Mater. Process. Technol.* **2008**, *198*, 226–233. [CrossRef]